Check for updates

Spatiotemporal monitoring of intracellular metabolic dynamics by resonance Raman microscopy with isotope labeling†

Yusuke Yonamine, ID *[a] Kotaro Hiramatsu, ID [bcd] Takuro Ideguchi, ID [cde] Takuro Ito, ID [f] Tomomi Fujiwara,[g] Yoshiko Miura, ID [g] Keisuke Goda ID [bfhi] and Yu Hoshino ID *[g]

Cellular metabolites are valuable in a diverse range of applications. For example, the unicellular green alga *Haematococcus lacustris* produces as a secondary metabolite the carotenoid pigment astaxanthin (AXT), which is widely used in nutraceutical, cosmetic, and food industries due to its strong antioxidant activity. In order to enhance the productivity of *H. lacustris*, spatial and temporal understanding of its metabolic dynamics is essential. Here we show spatiotemporal monitoring of AXT production in *H. lacustris* cells by resonance Raman microscopy combined with stable isotope labeling. Specifically, we incorporated carbon dioxide ($^{13}CO_2$) labeled with a stable isotope (^{13}C) into *H. lacustris* cells through carbon fixation and traced its conversion to ^{13}C-AXT using our resonance Raman microscope. We incubated *H. lacustris* cells under various conditions by switching, pulsing, and replacing $^{13}CO_2$ and $^{12}CO_2$. By measurement of these cells we determined the fixation time of ^{13}C-carbon, visualized the intracellular localization of ^{13}C- and ^{12}C-AXTs, and revealed the dynamic consumption–production equilibrium of the accumulated AXT. This work is a valuable step in the development of effective screening criteria for high AXT-producing *H. lacustris* cells.

Introduction

The observation and analysis of intracellular dynamics is essential to the study of cell biology.[1–6] For example, organelles undergo dynamic morphological changes during autophagy[1] or cell death[2] by apoptosis or necrosis. Microtubules[3] and nucleolus[4] form a wide range of spatial configurations in cell-cycle transitions including cell division, differentiation, and morphogenesis. Mitochondria mount metabolic defenses against intracellular pathogens in response to infection.[5,6] Beyond basic science, cellular metabolites produced by animal cells and microbes are widely used in the pharmaceutical, nutraceutical, cosmetic, and food industries,[7–10] and increasing metabolite production efficiency by cell engineering remains a major goal. For instance, antibodies produced by Chinese Hamster Ovary (CHO) cells are used as therapeutic agents,[7] and secondary metabolites produced by microalgae cells are used as biofuels[8,9] and nutritional supplements.[10] Metabolic fluxes in a living cell are highly regulated and varied in response to environmental changes, bioactive substances, and transitions of the cell cycle. Accordingly, the spatiotemporal observation of intracellular metabolic dynamics, including production, accumulation, and transportation, is foundational to the understanding of cellular metabolism. It is also effective for developing screening criteria for applications such as those above as well as for regenerative medicine and cell therapy.[11–13]

Fluorescence microscopy, with the help of fluorescent probes,[14,15] is widely used to identify the intracellular localization and distribution of metabolites with subcellular resolution. However, such fluorescent labeling inevitably comes with several fundamental drawbacks when observing intracellular metabolic dynamics. First, the hydrophobicity of small-molecule fluorescent probes[16] and the bulkiness of fluorescent protein labels[17,18] often disturb natural biological functions and

[a]Research Institute for Electronic Science, Hokkaido University, Kita 21, Nishi 10, Kita-ku, Sapporo 001-0021, Japan. E-mail: yonamine@poly.es.hokudai.ac.jp

[b]Department of Chemistry, The University of Tokyo, 7-3-1 Hongo, Bunkyo-ku, Tokyo 113-0033, Japan

[c]Research Centre for Spectrochemistry, The University of Tokyo, 7-3-1 Hongo, Bunkyo-ku, Tokyo 113-0033, Japan

[d]PRESTO, Japan Science and Technology Agency, 7-3-1 Hongo, Bunkyo-ku, Tokyo 113-0033, Japan

[e]Institute for Photon Science and Technology, The University of Tokyo, 7-3-1 Hongo, Bunkyo-ku, Tokyo 113-0033, Japan

[f]Japan Science and Technology Agency, 4-1-8 Honcho, Kawaguchi-shi, Saitama 332-0012, Japan

[g]Department of Chemical Engineering, Kyushu University, 744 Motooka, Fukuoka 819-0395, Japan. E-mail: yhoshino@chem-eng.kyushu-u.ac.jp

[h]Institute of Technological Sciences, Wuhan University, Hubei 430072, China

[i]Department of Bioengineering, University of California, Los Angeles, California 90095, USA

† Electronic supplementary information (ESI) available: Experimental section and supporting figures. See DOI: 10.1039/d0ra02803g

lead to cellular toxicity. Second, intracellular fluorescent staining with fluorescent dyes suffers from non-specific binding and misdistribution, leading to potential errors in quantitative live imaging.[19,20] Third, sequential labelling such as pulse-chase analysis using protein tags[21] is not applicable to the study of small metabolites. For these reasons, fluorescence microscopy is not always suitable for monitoring intracellular metabolic dynamics.

On the other hand, Raman microscopy together with stable isotope (SI) labeling[22–37] provides significant advantages in monitoring intracellular metabolite dynamics. First, since SI probes can be incorporated and metabolized in cells similarly to the original substrates, their use does not lead to cellular toxicity, interference with biological functions, or non-specific binding. Second, the metabolic process from incorporation to production can be tracked by exposing cells to an SI-labeled substrate and detecting SI-labeled products. Third, by analysis of the peaks of Raman spectra, Raman mapping quantifies the ratio of SI-labeled products to unlabeled products at spatial positions of interest. Though Raman microscopy with SI-labeled substrates has revealed the cellular anabolic processes of biopolymers including proteins,[24–31] DNAs,[26–28] and lipid droplets,[32–35] the spatiotemporal dynamics of secondary metabolites has not been monitored to date despite the usefulness of these metabolites in a wide range of applications.[38–41]

In this paper, we show spatiotemporal monitoring of intracellular metabolic dynamics, for screening the production of secondary metabolites, using resonance Raman microscopy with an SI-labeled substrate exposed to various conditions (Fig. 1). Specifically, we investigated the biosynthesis process of a commercially valuable carotenoid, astaxanthin (AXT), produced by the unicellular photosynthetic alga *Haematococcus lacustris*,[42] a species known to accumulate AXT under induced stress, usually accompanied by a drastic morphological transformation from green motile cells to red non-motile cyst cells.[43] While fluorescence from AXT is weak,[44] resonance Raman microscopy can provide an enhanced Raman signal from AXT[45–48] and can be used to selectively identify AXT in single *H. lacustris* cells from their primary cellular constituents including proteins, nucleotides, and lipids. We incorporated carbon dioxide ($^{13}CO_2$) labeled by an SI (^{13}C) into *H. lacustris* cells through carbon fixation and traced its conversion to ^{13}C-AXT by resonance Raman microscopy with the SI. We incubated *H. lacustris* cells under various conditions by switching, pulsing, and replacing $^{13}CO_2$ and $^{12}CO_2$. By measurement of these cells
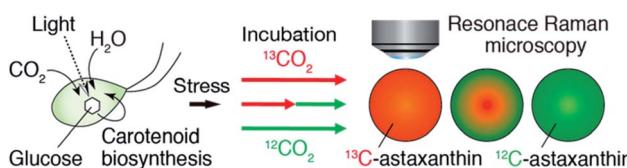
we determined the fixation time of ^{13}C-carbon, visualized the intracellular localization of ^{13}C- and ^{12}C-AXTs, and revealed the dynamic consumption–production equilibrium of the accumulated AXT. We believe this work represents a valuable step in the development of effective screening criteria for high AXT-producing *H. lacustris* cells.

Results and discussion

Resonance Raman imaging of *H. lacustris* cells accumulating ^{13}C-AXT

First, we performed resonance Raman imaging of *H. lacustris* cells incubated with $^{13}CO_2$ long enough for $^{13}CO_2$ to convert to ^{13}C-AXT. We induced intracellular production of AXT for 5 days under nitrogen deficiency and strong light irradiation and measured the resonance Raman spectra of the cells. We obtained typical resonance Raman spectra of carotenoids including ν_1–ν_4 peaks from the resultant red cyst cells (Fig. 2a, red).[43] The ν_1–ν_4 peaks are assigned to vibrational modes as follows: ν_1, C=C stretching; ν_2, C–C stretching/C–H in-plane bending; ν_3, CH_3 rocking; ν_4, C–H out-of-plane wagging.[45,49] Spectra consist mainly of peaks corresponding to AXT, as it is the major ingredient (>90%) of carotenoid production by *H. lacustris* cells.[50] The AXT spectra of cells incubated with $^{13}CO_2$ are shifted to lower wavenumbers compared to those of cells incubated with $^{12}CO_2$ (Fig. 2a). This red shift is attributed to the substitution of ^{12}C by the heavier isotope ^{13}C, resulting in a lower frequency of molecular vibration. In particular, large shifts were observed in ν_1 and ν_2 peaks, which are assigned to vibrational modes of carbon–carbon bonds. The largest shift (32 cm^{-1}) was observed in the ν_1 peak, which shifted from 1518 cm^{-1} (^{12}C: green) to 1486 cm^{-1} (^{13}C: red). These results indicate that $^{13}CO_2$ was incorporated into *H. lacustris* cells through carbon fixation and that ^{13}C-carbon was converted to AXT through the non-mevalonate pathway and subsequent carotenogenesis.[51]

We then demonstrated discrimination of *H. lacustris* cells accumulating ^{13}C- or ^{12}C-AXT by resonance Raman imaging
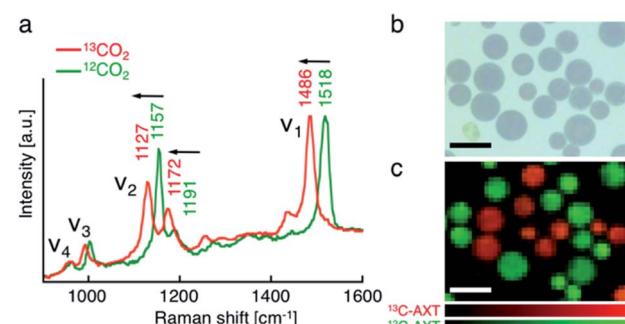
Fig. 2 Resonance Raman spectroscopy of mixed *H. lacustris* cells that accumulate ^{13}C- or ^{12}C-AXT. (a) Resonance Raman spectra of intracellular AXT. Red: cells incubated with $^{13}CO_2$. Green: cells incubated with $^{12}CO_2$. (b) Bright-field image of the mixed cells. (c) Resonance Raman image of the mixed cells. ^{13}C- and ^{12}C-AXT are color-coded in red (^{13}C) and green (^{12}C), respectively. Scale bars: 40 µm. Color bars: intensities of Raman spectra of ^{13}C- (red) and ^{12}C-AXT (green).

Fig. 1 Schematic of our approach. We monitored the production of AXT in a single *H. lacustris* cell by resonance Raman microscopy with $^{13}CO_2$ and $^{12}CO_2$ incubation.

based on the spectral shift. We mixed in equal number *H. lacustris* cells that accumulated ^{13}C- and those that accumulated ^{12}C-AXT, and then analyzed the cell mixture by Raman mapping. Raman images were generated by classical least squares modeling of the ^{13}C- and ^{12}C-AXT spectra obtained during the long-term induction. At each image pixel position, a linear combination of factors was calculated to estimate the measured spectrum. ^{13}C- and ^{12}C-AXT in the images were color-coded as red and green, respectively. As a result, the two types of cells were clearly discriminated (Fig. 2c). This result shows the advantage of Raman imaging over bright field microscopy (Fig. 2b) for detecting targets labeled with stable isotopes.

Resonance Raman spectroscopy of *H. lacustris* cells incubated with a mixture of $^{13}CO_2$ and $^{12}CO_2$

Second, we investigated the resonance Raman spectral shift of AXT in *H. lacustris* cells incubated with $^{13}CO_2$ and $^{12}CO_2$ mixed in various ratios. We induced production of AXT in the cells under various $^{13}CO_2$ ratios ($^{13}CO_2$: 0, 25, 50, 75, and 100 vol%) for 24 h (Fig. 3a). The Raman peaks of AXT (ν_1 and ν_2) gradually shifted toward lower wavenumber positions as the $^{13}CO_2$ ratio increased (Fig. 3b). When plotting the ratio of $^{13}CO_2$ *versus* the wavenumber of each peak (ν_1, ν_{2a}, and ν_{2b}), all showed a linear relationship (Fig. 3c). The slope (m) of the ν_1 peak, attributed to C=C stretching, has a larger absolute value (ν_1: $m = -0.33$) than that of the ν_2 peaks, which include a contribution from C–C stretching (ν_{2a}: $m = -0.25$, ν_{2b}: $m = -0.22$). These results are congruent with observed resonance Raman spectral shifts of carotenoids (mainly β-carotene) in cyanobacterial cells incubated with a ^{13}C source.[22] *H. lacustris* cells fix $^{13}CO_2$ and $^{12}CO_2$

gases with equal probability, since stable isotopes have the same biochemical properties.[52] Consequently, the carbon ratio of ^{13}C and ^{12}C in an AXT molecule produced in a cell is presumably the same as the ratio of $^{13}CO_2$ and $^{12}CO_2$ in the culturing atmosphere. On the other hand, the ratio of the ^{13}C carbon–carbon bond wavenumber ($\sigma_{^{13}C}$) to the ^{12}C carbon–carbon bond wavenumber ($\sigma_{^{12}C}$) corresponds to the square root of the ratio of the reduced masses, given that the wavenumber is defined as: $\sigma = \sqrt{k}/2\pi c\sqrt{\mu}$, where k is the spring constant of the corresponding chemical bond and μ is the reduced mass.[30] In fact, all of the ratios of resonance Raman peaks ($\sigma_{^{13}C\text{-}100\%}/\sigma_{^{12}C\text{-}100\%}$) are constant ($\nu_1$, 0.979; ν_{2a}, 0.983; ν_{2b}, 0.978; Fig. 3b and c) and approximately consistent with the theoretical value ($\sigma_{^{13}C}/\sigma_{^{12}C} = 0.960$). These results show that the resonance Raman spectra of AXT in *H. lacustris* cells incubated with a mixture of $^{13}CO_2$ and $^{12}CO_2$ shift to lower wavenumbers in a linear manner corresponding to the $^{13}CO_2$ ratio in the culturing atmosphere.

Resonance Raman imaging of *H. lacustris* cells incubated with atmosphere switching from $^{13}CO_2$ to $^{12}CO_2$

Third, we switched the incubation atmosphere from $^{13}CO_2$ to $^{12}CO_2$ during AXT induction, and then investigated the ratios of ^{13}C- and ^{12}C-AXT in *H. lacustris* cells by resonance Raman imaging. We varied the time to switch from $^{13}CO_2$ to $^{12}CO_2$ during the 24 h incubation period to investigate cells incubated with $^{13}CO_2$ for 12 h, 15 h, 18 h, 21 h, and 24 h (Fig. 4a). In most cases, resonance Raman spectra of the *H. lacustris* cells were a superposition of the ^{13}C-AXT spectrum (peaks: ν_2, 1128 cm^{-1} and 1173 cm^{-1}; ν_1, 1484 cm^{-1}; in red) and the ^{12}C-AXT spectrum (peaks: ν_2, 1156 cm^{-1} and 1192 cm^{-1}; ν_1, 1514 cm^{-1}; in green) with varying intensities of the two spectra (representative four spectra are shown in Fig. 4b). This is in contrast to the gradual red shift observed in spectra of cells incubated with a mixture of $^{13}CO_2$ and $^{12}CO_2$ (Fig. 3). The results of this atmosphere switching experiment indicate that cells contain both 100% ^{13}C-AXT and 100% ^{12}C-AXT in various proportions, with no or a negligible amount of AXT molecules composed of both ^{13}C- and ^{12}C-carbons. This can be attributed to the rapid conversion rate from carbon source to AXT molecule, due to the small molecular size of AXT. In other words, after switching from $^{13}CO_2$ to $^{12}CO_2$, the ^{13}C-carbon source was consumed rapidly for AXT production, and then the carbon source quickly switched to ^{12}C-carbon, resulting in productions of 100% ^{13}C-AXT and 100% ^{12}C-AXT. In resonance Raman images generated by the classical least squares modeling of the ^{13}C- and ^{12}C-AXT spectra, *H. lacustris* cells are represented as a gradation of red (^{13}C-AXT) and green (^{12}C-AXT) in an RGB color model (*e.g.*, Cell 1, yellow-green; Cell 2, yellow; Cell 3, orange; Cell 4, red-orange; Fig. 4b), since they include both 100% ^{13}C-AXT and 100% ^{12}C-AXT. On the other hand, AXT inside of a cell was distributed non-uniformly, suggesting that the AXT-accumulation process was still in a transition period to maturation after AXT-induction at 24 h (Fig. 4b). Notably, localization of ^{13}C-AXT (red) and ^{12}C-AXT (green) was observed inside some cells (Fig. S1†), revealing the progression of carbon fixation and conversion to AXT.
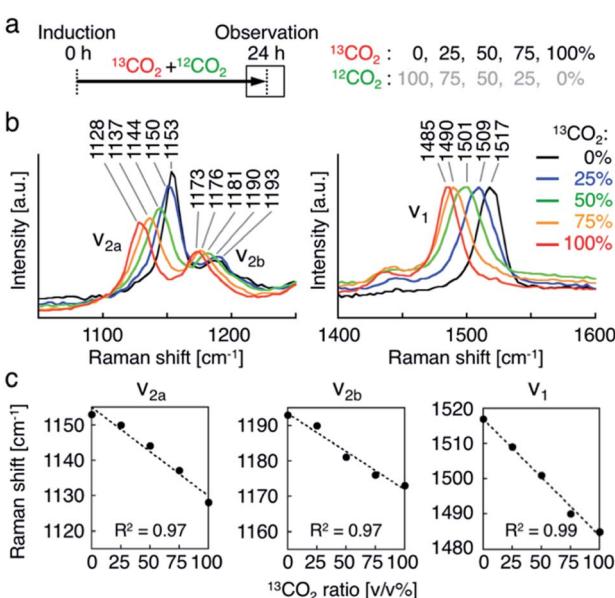
Fig. 3 Resonance Raman spectroscopy of *H. lacustris* cells incubated with mixture of $^{13}CO_2$ and $^{12}CO_2$. (a) Incubation timeline of *H. lacustris* cells with $^{13}CO_2$ and $^{12}CO_2$ gases mixed at various ratios. (b) Resonance Raman spectra of *H. lacustris* cells incubated at various $^{13}CO_2$ ratios. (c) Raman shifts of the peaks (ν_{2a}, ν_{2b}, ν_1) against the ratio of $^{13}CO_2$ in the incubation atmosphere.
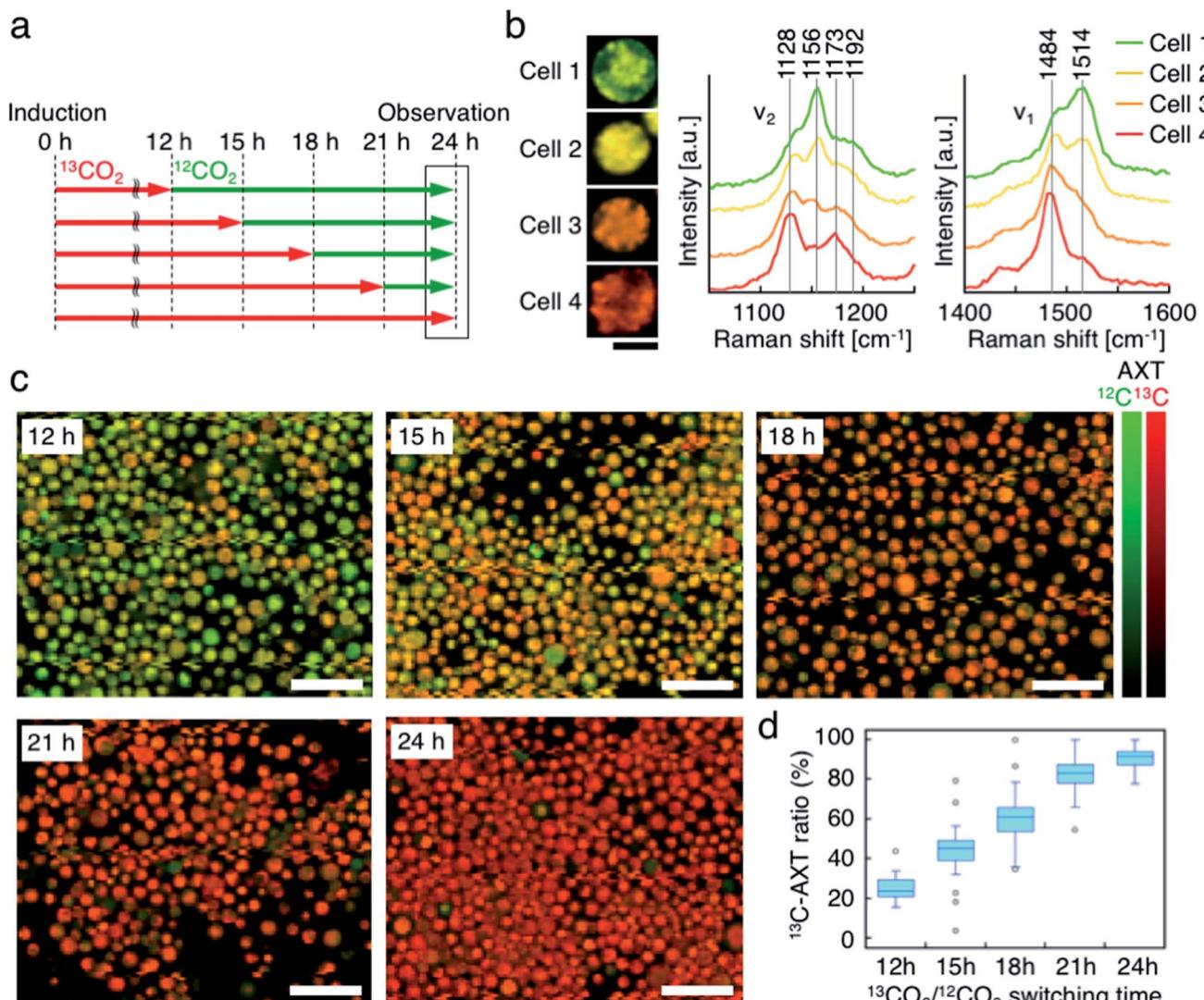
Fig. 4 Resonance Raman imaging of *H. lacustris* cells incubated with atmosphere switching from $^{13}CO_2$ to $^{12}CO_2$. (a) Incubation timeline of *H. lacustris* cells with incubation switching from $^{13}CO_2$ to $^{12}CO_2$ at various timings. (b) Resonance Raman images and spectra of *H. lacustris* cells that accumulate both ^{13}C- and ^{12}C-AXT. ^{13}C- and ^{12}C-AXT are color-coded in red (^{13}C) and green (^{12}C), respectively. Cell 1, 12 h; Cell 2, 15 h; Cell 3, 15 h; Cell 4, 18 h. Scale bars: 20 μm. (c) Low-magnification resonance Raman images of *H. lacustris* cells. Red, ^{13}C-AXT; green, ^{12}C-AXT. Scale bars: 100 μm. Color bars: intensities of Raman spectra of ^{13}C- (red) and ^{12}C-AXT (green). (d) Box-and-whisker plot of ^{13}C-AXT ratios in the resonance Raman spectra of *H. lacustris* cells ($n = 30$).

We then observed the *H. lacustris* cells with low-magnification resonance Raman images and investigated the comprehensive changes of ^{13}C-AXT in the cells (Fig. 4c). As the incubation time with $^{13}CO_2$ increased, green color (^{12}C-AXT) decreased and red color (^{13}C-AXT) increased, as observed in resonance Raman images of cells incubated with $^{13}CO_2$ for 12 h, 15 h, 18 h, and 21 h (Fig. 4c). This gradual change in color indicates that *H. lacustris* cells have CO_2 fixation activity during the 12 h to 21 h period and then complete the conversion to AXT by the end of the incubation (24 h). On the other hand, comparing the images at 21 h and 24 h, no significant color change is observed, showing only red color (^{13}C-AXT) without green color (^{12}C-AXT). This result indicates that the conversion process from $^{12}CO_2$ fixation to ^{12}C-AXT production was

incomplete during this period (21–24 h). In order to quantitatively support this, we measured resonance Raman spectra of 30 cells (at the center of the cells) randomly selected from individual images and calculated the ^{13}C-AXT ratios by spectral separation using a multivariate curve resolution–alternating least squares (MCR-ALS) algorithm (Fig. 4d). From these spectra, we confirmed that ^{13}C-AXT accumulated until 21 h and became saturated afterwards. We then investigated the activity of CO_2 fixation and AXT production after 24 h. After 24 h of $^{13}CO_2$, the incubation atmosphere was switched from $^{13}CO_2$ to $^{12}CO_2$ at 6 hour intervals, and the total AXT-induction time was 48 h (Fig. S2a†). In these cases, accumulation rate of ^{13}C-AXT decreased (Fig. S2b and c†), which indicates that the conversion activity from 24 h to 48 h was lower than that of the 12 h to

24 h period. As demonstrated above, the active conversion period from CO_2 fixation to AXT production can be probed by switching from $^{13}CO_2$ to $^{12}CO_2$ at various times and comparing the difference of ^{13}C- or ^{12}C-AXT accumulation by resonance Raman imaging.

Resonance Raman imaging of ^{13}C-AXT in *H. lacustris* cells labeled by pulse incubation with $^{13}CO_2$

Fourth, we labeled AXT in *H. lacustris* cells by pulse incubation, where the duration of incubation with $^{13}CO_2$ was shorter, and detected ^{13}C-AXT by resonance Raman imaging to specify the carbon fixation time. In the aforementioned incubations with the switching of $^{13}CO_2$ to $^{12}CO_2$, whether $^{13}CO_2$ was fixed at earlier or later times could not be determined, since the ^{13}C-AXT indicated by the red color accumulated during the $^{13}CO_2$ incubation. In this experiment, we incubated the cells with $^{13}CO_2$ for a constant "pulse" of time (9 h), with the remaining incubation under $^{12}CO_2$ (15 h), for a total AXT induction time of 24 h. The $^{13}CO_2$ pulse incubations were shifted by 3 h in the timeline (Fig. 5a) to probe the carbon fixation time. We calculated the ^{13}C-AXT ratios of 30 cells randomly selected for each $^{13}CO_2$ pulse timing (Fig. 5b). The plot shows that $^{13}CO_2$ fixation and the resultant ^{13}C-AXT production are significantly higher in the late ^{13}C-induction phases ((iv) 9–18 h, (v) 12–21 h, (vi) 15–24 h), while both are lower in the early ^{13}C-induction phases ((i) 0–9 h, (ii) 3–12 h, (iii) 6–15 h). Notably, there is a large gap between

conditions (iii) and (iv), indicating that CO_2 is actively fixed and converted into AXT after 15 h. Among the late pulse incubations, conditions (v) and (vi) show higher ^{13}C-AXT ratios than condition (iv) (*t*-test; $p < 0.05$), whereas no significant difference was observed (*t*-test; $p = 0.20$) between (v) and (vi). These results indicate that the activity of carbon-fixation and conversion is high during the 15 to 21 h period of incubation.

We then compared the ^{13}C-AXT ratios of *H. lacustris* cells in the same resonance Raman image frame. We represent only ^{13}C-AXT in pseudo color (Fig. 5c) to highlight ^{13}C-carbon fixed during the pulse incubation, rather than representing both ^{13}C-AXT (red) and ^{12}C-AXT (green) in the RGB color model (Fig. S3a†). Cells that actively fixed $^{13}CO_2$ and converted it to ^{13}C-AXT are clearly detected in the image of condition (v) 12–21 h, while such cells were scarcely observed in the image of condition (i) 0–9 h or the image of the control condition, which was incubation under only $^{12}CO_2$. These results demonstrate that this method of pulse incubation can be useful for screening active *H. lacustris* cells which show a high efficiency of carbon-fixation and AXT-conversion.

Resonance Raman imaging of *H. lacustris* cells after replacing ^{13}C-AXT by ^{12}C-AXT by $^{12}CO_2$ incubation

Lastly, we accumulated ^{13}C-AXT in *H. lacustris* cells and then replaced it with ^{12}C-AXT by incubating the cells under $^{12}CO_2$.
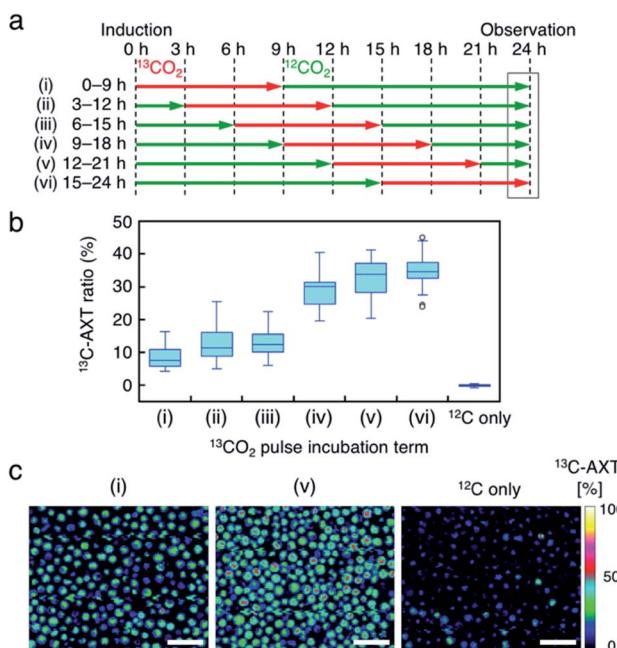

Fig. 5 Resonance Raman imaging of ^{13}C-AXT in *H. lacustris* cells labeled by pulse incubation with $^{13}CO_2$. (a) Incubation timeline of *H. lacustris* cells with $^{13}CO_2$ incubation pulsed (9 h) at various timings in 24 h. (b) Box-and-whisker plot of ^{13}C-AXT ratios in the resonance Raman spectra of *H. lacustris* cells ($n = 30$). ^{12}C shows a control culture with $^{12}CO_2$ incubation. (c) Low-magnification resonance Raman images of *H. lacustris* cells. The ratio of ^{13}C-AXT is represented in pseudo-color. Scale bars: 100 μm.
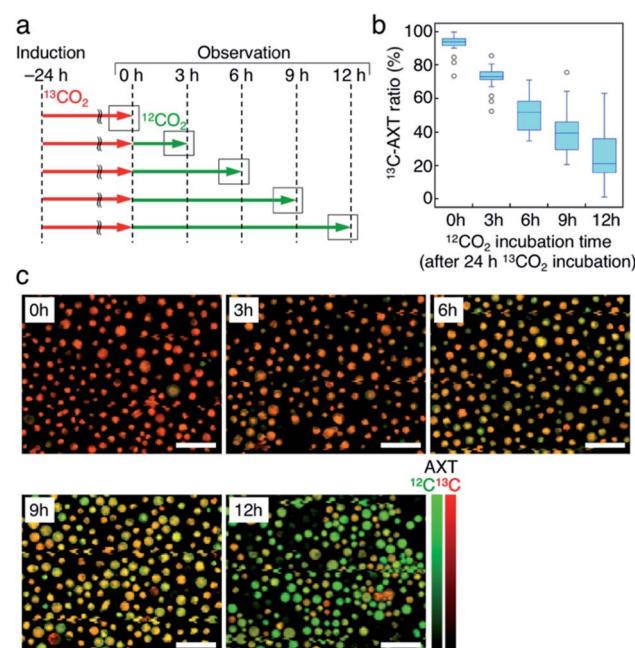
Fig. 6 Resonance Raman imaging of replacing ^{13}C-AXT by ^{12}C-AXT in *H. lacustris* cells by incubating with $^{12}CO_2$. (a) Incubation timeline of *H. lacustris* cells with $^{12}CO_2$ incubation following 24 hours of $^{13}CO_2$ incubation. (b) Box-and-whisker plot of ^{13}C-AXT ratios in the resonance Raman spectra of *H. lacustris* cells ($n = 30$). (c) Low-magnification resonance Raman images of *H. lacustris* cells. ^{13}C- and ^{12}C-AXT are color-coded in red (^{13}C) and green (^{12}C), respectively. Scale bars: 100 μm. Color bars: intensities of Raman spectra of ^{13}C- (red) and ^{12}C-AXT (green).
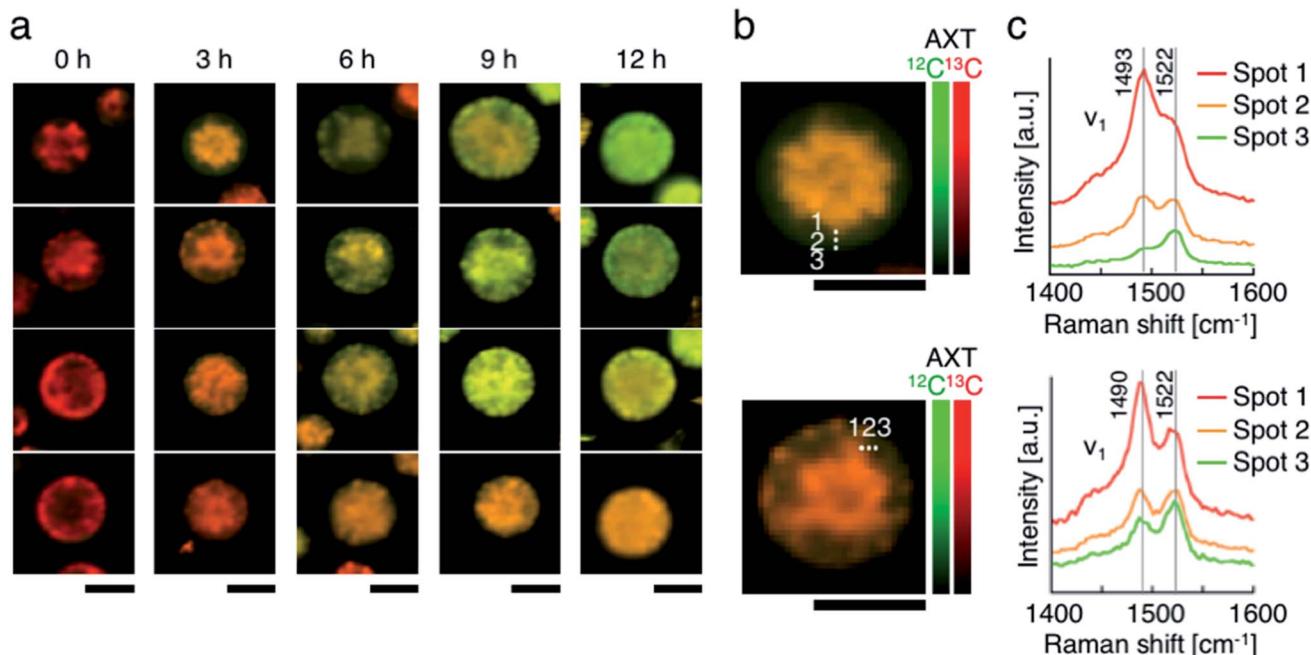
Fig. 7 Resonance Raman imaging of the heterogeneity of ^{13}C-AXT and ^{12}C-AXT in a single *H. lacustris* cell. (a) Resonance Raman images of *H. lacustris* cells incubated with ^{12}CO$_2$ after incubation with ^{13}CO$_2$. The incubation conditions used here are identical to those in Fig. 6(b and c). Magnified resonance Raman images (b) and spectra (c) of *H. lacustris* cells incubated with ^{12}CO$_2$ for 3 h after their accumulation of ^{13}C-AXT. The spectra correspond to the spots in the images of (b). ^{13}C- and ^{12}C-AXT are color-coded in red (^{13}C) and green (^{12}C), respectively. Scale bars: 20 μm. Color bars: intensities of Raman spectra of ^{13}C- (red) and ^{12}C-AXT (green).

We induced ^{13}C-AXT production in *H. lacustris* cells for 24 h by incubation under ^{13}CO$_2$ and then replaced the atmosphere with ^{12}CO$_2$ for different durations (3 h increments) before observation (Fig. 6a). Calculation of the ^{13}C-AXT ratios of 30 cells randomly selected for each condition showed a large dispersion of ^{13}C-AXT ratios, which reflects the difference in ^{12}C-AXT production activity among the cells (Fig. 6b). Interestingly, we observed that ^{13}C-AXT in some cells was completely replaced with ^{12}C-AXT after 12 h (Fig. 6b and c), suggesting that AXT is in dynamic equilibrium between consumption and production. This information on carbon flow cannot be obtained by merely detecting non-labeled AXT and thus demonstrates the advantage of combining resonance Raman imaging with ^{13}C-labeling. Furthermore, we observed heterogeneity of ^{13}C-AXT (red) and ^{12}C-AXT (green) in a single cell after incubation with ^{12}CO$_2$, but the AXTs became homogenized as the time of incubation with ^{12}CO$_2$ was extended (Fig. 7). Specifically, ^{12}C-AXT infiltrated from the edge of the cell towards its center (Fig. 7a). In fact, the resonance Raman spectra around the cell periphery confirmed that the ratio of ^{12}C-AXT was high at the edge and low at the center (Fig. 7b). This observation can be attributed to the transportation of newly produced ^{12}C-AXT precursors to lipid droplets around the center.[53,54] In an intermediate cell during encystment, chloroplasts, which produce an AXT precursor, are located around the cell periphery, while oil droplets, which serve as a "sink" for AXT, are located around the nucleus at the center.[53,54] The newly produced 100% ^{12}C-AXT precursors are delivered to the oil droplets from the periphery, converted to ^{12}C-AXT by an enzyme inside, and mixed with pre-existing 100%

^{13}C-AXT. Consequently, a gradient of ^{12}C-AXT and ^{13}C-AXT forms, causing heterogeneity in a single cell. These results demonstrate that the distribution of AXTs produced at different times can be visualized in a single cell by resonance Raman imaging combined with ^{13}C- and ^{12}C-labeling.

Conclusions

In this paper, we demonstrated spatiotemporal monitoring of AXT production in *H. lacustris* cells, incubated under varying ^{13}CO$_2$ and ^{12}CO$_2$ atmospheric conditions, by resonance Raman imaging. First, we induced AXT production in *H. lacustris* by incubating the cells with ^{13}CO$_2$ for enough time to produce ^{13}C-AXT, the resonance Raman spectrum of which shows red shifts compared to that of ^{12}C-AXT. This result shows that ^{13}CO$_2$ was incorporated into *H. lacustris* cells through carbon fixation and that ^{13}C-carbon was converted to AXT through cellular metabolism. Based on the spectral difference between ^{13}C- and ^{12}C-AXT, we clearly discriminated *H. lacustris* cells accumulating ^{13}C- or ^{12}C-AXT by resonance Raman imaging. Second, we investigated the resonance Raman spectral shift of AXT in *H. lacustris* cells when incubated with a mixture of ^{13}CO$_2$ and ^{12}CO$_2$ gases in various ratios. We observed that the resonance Raman spectra shifted to positions at lower wavenumbers in a linear manner corresponding to the ^{13}CO$_2$ ratio of the culturing atmosphere. Third, we switched the incubation atmosphere from ^{13}CO$_2$ to ^{12}CO$_2$ at various times and then investigated the ratios of ^{13}C- and ^{12}C-AXT in the cells by resonance Raman imaging. The results indicated that the cells

contained both 100% ^{13}C-AXT and 100% ^{12}C-AXT in various proportions. By comparing *via* resonance Raman imaging the differences in ^{13}C- and ^{12}C-AXT accumulation, the active conversion period from CO_2 fixation to AXT production could be probed. Fourth, we labeled AXT with ^{13}C by incubating cells under $^{13}CO_2$ for short pulses of time, to specify the active time of carbon fixation and conversion. Lastly, we accumulated ^{13}C-AXT in *H. lacustris* cells in advance and subsequently replaced it with ^{12}C-AXT by incubating the cells under $^{12}CO_2$ for different durations. We observed a high variation between cells in the rate at which ^{13}C-AXT decreased, reflecting individual differences in ^{12}C-AXT production activity among cells. In some cells, ^{13}C-AXT was completely replaced with ^{12}C-AXT, suggesting that AXT is in dynamic equilibrium between consumption and production. Furthermore, localizations of ^{13}C-AXT and ^{12}C-AXT in a single cell were observed by magnified resonance Raman imaging.

Our method provides spatiotemporal information for single cells, including the conversion process from substrate to metabolite, the distribution process of the metabolite, and the turnover of the metabolite in dynamic equilibrium. By virtue of non-cytotoxic labelling and non-invasive imaging, long-term monitoring of metabolic dynamics in living cells can be achieved. Furthermore, by integrating our method with technologies for single cell isolation,[55,56] the intracellular metabolism of an identified cell can be monitored. When combined with state-of-the-art Raman spectroscopy techniques that have higher spatiotemporal resolution, such as stimulated Raman scattering (SRS)[57–60] or coherent anti-Stokes Raman scattering (CARS),[61–63] the process of metabolite distribution can be monitored in a single cell with further detail. Leveraging such information for biotechnological production of target metabolites could provide significant value in terms of productivity. Furthermore, using Raman-activated cell sorting (RACS)[64–66] will enable screening for cells with high metabolite productivity from a genetically diverse cell population.

Conflicts of interest

There are no conflicts to declare.

Acknowledgements

References

1 N. Mizushima, T. Yoshimori and B. Levine, *Cell*, 2010, **140**, 313–326.

2 O. Kepp, L. Galluzzi, M. Lipinski, J. Yuan and G. Kroemer, *Nat. Rev. Drug Discovery*, 2011, **10**, 221–237.

3 J. Zenker, M. D. White, R. M. Templin, R. G. Parton, O. Thorn-Seshold, S. Bissiere and N. Plachta, *Science*, 2017, **357**, 925–928.

4 A. Sakaue-Sawano, H. Kurokawa, T. Morimura, A. Hanyu, H. Hama, H. Osawa, S. Kashiwagi, K. Fukami, T. Miyata, H. Miyoshi, T. Imamura, M. Ogawa, H. Masai and A. Miyawaki, *Cell*, 2008, **132**, 487–498.

5 L. Pernas, C. Bean, J. C. Boothroyd and L. Scorrano, *Cell Metab.*, 2018, **27**, 886–897.e4.

6 T. Yoshizumi, T. Ichinohe, O. Sasaki, H. Otera, S. Kawabata, K. Mihara and T. Koshiba, *Nat. Commun.*, 2014, **5**, 4713.

7 J. Y. Kim, Y. G. Kim and G. M. Lee, *Appl. Microbiol. Biotechnol.*, 2012, **93**, 917–930.

8 M. S. Cooper, W. R. Hardin, T. W. Petersen and R. A. Cattolico, *J. Biosci. Bioeng.*, 2010, **109**, 198–201.

9 K. Yamada, H. Suzuki, T. Takeuchi, Y. Kazama, S. Mitra, T. Abe, K. Goda, K. Suzuki and O. Iwata, *Sci. Rep.*, 2016, **6**, 26327.

10 M. A. Borowitzka, *J. Appl. Phycol.*, 2013, **25**, 743–756.

11 J. Nielsen and J. D. Keasling, *Cell*, 2016, **164**, 1185–1197.

12 J. C. Caicedo, S. Cooper, F. Heigwer, S. Warchal, P. Qiu, C. Molnar, A. S. Vasilevich, J. D. Barry, H. S. Bansal, O. Kraus, M. Wawer, L. Paavolainen, M. D. Herrmann, M. Rohban, J. Hung, H. Hennig, J. Concannon, I. Smith, P. A. Clemons, S. Singh, P. Rees, P. Horvath, R. G. Linington and A. E. Carpenter, *Nat. Methods*, 2017, **14**, 849–863.

13 K. D. Piatkevich, E. E. Jung, C. Straub, C. Linghu, D. Park, H. J. Suk, D. R. Hochbaum, D. Goodwin, E. Pnevmatikakis, N. Pak, T. Kawashima, C. T. Yang, J. L. Rhoades, O. Shemesh, S. Asano, Y. G. Yoon, L. Freifeld, J. L. Saulnier, C. Riegler, F. Engert, T. Hughes, M. Drobizhev, B. Szabo, M. B. Ahrens, S. W. Flavell, B. L. Sabatini and E. S. Boyden, *Nat. Chem. Biol.*, 2018, **14**, 352–360.

14 J. W. Lichtman and J. A. Conchello, *Nat. Methods*, 2005, **2**, 910–919.

15 Z. Liu, L. D. Lavis and E. Betzig, *Mol. Cell*, 2015, **58**, 644–659.

16 L. Wang, M. S. Frei, A. Salim and K. Johnsson, *J. Am. Chem. Soc.*, 2019, **141**, 2770–2781.

17 H.-S. Liu, M.-S. Jan, C.-K. Chou, P.-H. Chen and N.-J. Ke, *Biochem. Biophys. Res. Commun.*, 1999, **260**, 712–717.

18 M. R. Depaoli, H. Bischof, E. Eroglu, S. Burgstaller, J. Ramadani-Muja, T. Rauter, M. Schinagl, M. Waldeck-Weiermair, J. C. Hay, W. F. Graier and R. Malli, *Pharmacol. Ther.*, 2019, **202**, 98–119.

19 M. C. Wang, W. Min, C. W. Freudiger, G. Ruvkun and X. S. Xie, *Nat. Methods*, 2011, **8**, 135–138.

20 S. Yamashiro, D. Taniguchi, S. Tanaka, T. Kiuchi, D. Vavylonis and N. Watanabe, *Biophys. J.*, 2019, **116**, 142–150.

21 A. Gautier, A. Juillerat, C. Heinis, I. R. Correa Jr, M. Kindermann, F. Beaufils and K. Johnsson, *Chem. Biol.*, 2008, **15**, 128–136.

22 M. Li, D. P Canniffe, P. J. Jackson, P. A. Davison, S. FitzGerald, M. J. Dickman, J. G. Burgess, C. N. Hunter and W. E. Huang, *ISME J.*, 2012, **6**, 875–885.

23 D. McIlvenna, W. E. Huang, P. Davison, A. Glidle, J. Coopera and H. Yin, *Lab Chip*, 2016, **16**, 1420–1429.

24 H. N. Noothalapati Venkata and S. Shigeto, *Chem. Biol.*, 2012, **19**, 1373–1380.

25 Y. Shen, F. Xu, L. Wei, F. Hu and W. Min, *Angew. Chem., Int. Ed.*, 2014, **53**, 5596–5599.

26 Y. Wang, Y. Ji, E. S. Wharfe, R. S. Meadows, P. March, R. Goodacre, J. Xu and W. E. Huang, *Anal. Chem.*, 2013, **85**, 10697–10701.

27 M. Li, W. E. Huang, C. M. Gibson, P. W. Fowler and A. Jousset, *Anal. Chem.*, 2013, **85**, 1642–1649.

28 P. Kubryk, J. S. Kölschbach, S. Marozava, T. Lueders, R. U. Meckenstock, R. Niessner and N. P. Ivleva, *Anal. Chem.*, 2015, **87**, 6622–6630.

29 H.-J. van Manen, A. Lenferink and C. Otto, *Anal. Chem.*, 2008, **80**, 9576–9582.

30 L. Wei, Y. Yu, Y. Shen, M. C. Wang and W. Min, *Proc. Natl. Acad. Sci. U. S. A.*, 2013, **110**, 11226–11231.

31 L. Wei, Y. Shen, F. Xu, F. Hu, J. K. Harrington, K. L. Targoff and W. Min, *ACS Chem. Biol.*, 2015, **10**, 901–908.

32 H.-J. van Manen, Y. M. Kraan, D. Roos and C. Otto, *Proc. Natl. Acad. Sci. U. S. A.*, 2005, **102**, 10159–10164.

33 D. Zhang, M. N. Slipchenko and J.-X. Cheng, *J. Phys. Chem. Lett.*, 2011, **2**, 1248–1253.

34 J. Li and J.-X. Cheng, *Sci. Rep.*, 2014, **4**, 6807.

35 F. Hu, L. Wei, C. Zheng, Y. Shen and W. Min, *Analyst*, 2014, **139**, 2312–2317.

36 D. Berry, E. Mader, T. K. Lee, D. Woebken, Y. Wang, D. Zhu, M. Palatinszky, A. Schintlmeister, M. C. Schmid, B. T. Hanson, N. Shterzer, I. Mizrahi, I. Rauch, T. Decker, T. Bocklitz, J. Popp, C. M. Gibson, P. W. Fowler, W. E. Huang and M. Wagner, *Proc. Natl. Acad. Sci. U. S. A.*, 2014, **112**, 194–203.

37 Y. Yonamine, Y. Suzuki, T. Ito, Y. Miura, K. Goda, Y. Ozeki and Y. Hoshino, *ChemBioChem*, 2017, **18**, 2063–2068.

38 M. A. Borowitzka, *J. Appl. Phycol.*, 1995, **7**, 3–15.

39 M. Donia and M. T. Hamann, *Lancet Infect. Dis.*, 2003, **3**, 338–348.

40 B. Singh, T. K. Bhat and B. Singh, *J. Agric. Food Chem.*, 2003, **51**, 5579–5597.

41 A. L. Demain, *Appl. Microbiol. Biotechnol.*, 1999, **52**, 455–463.

42 M. Guerin, M. E. Huntley and M. Olaizola, *Trends Biotechnol.*, 2003, **21**, 210–216.

43 S. Boussiba, *Physiol. Plant.*, 2000, **108**, 111–117.

44 K. Ukibe, T. Katsuragi, Y. Tani and H. Takagi, *FEMS Microbiol. Lett.*, 2008, **286**, 241–248.

45 B. Robert, *Photosynth. Res.*, 2009, **101**, 147–155.

46 A. Kaczor, K. Turnau and M. Baranska, *Analyst*, 2011, **136**, 1109–1112.

47 A. M. Collins, H. D. Jones, D. Han, Q. Hu, T. E. Beechem and J. A. Timlin, *PLoS One*, 2011, **6**, e24302.

48 S. R. Fagerer, T. Schmid, A. J. Ibanez, M. Pabst, R. Steinhoff, K. Jefimovs, P. L. Urban and R. Zenobi, *Analyst*, 2013, **138**, 6732–6736.

49 S. Sato and M. Tasumi, *J. Raman Spectrosc.*, 1983, **14**, 310–321.

50 L. Recht, N. Topfer, A. Batushansky, N. Sikron, Y. Gibon, A. Fait, Z. Nikoloski, S. Boussiba and A. Zarka, *J. Biol. Chem.*, 2014, **289**, 30387–30403.

51 K. Grunewald, J. Hirschberg and C. Hagen, *J. Biol. Chem.*, 2001, **276**, 6023–6029.

52 B. Koletzko, T. Sauerwald and H. Demmelmair, *Eur. J. Pediatr.*, 1997, **156**, S12–S17.

53 U. Pick, A. Zarka, S. Boussiba and L. Davidi, *Planta*, 2019, **249**, 31–47.

54 M. Wayama, S. Ota, H. Matsuura, N. Nango, A. Hirata and S. Kawano, *PLoS One*, 2013, **8**, e53618.

55 A. E. Vasdekis and G. Stephanopoulos, *Metab. Eng.*, 2015, **27**, 115–135.

56 N. Ota, Y. Yonamine, T. Asai, Y. Yalikun, T. Ito, Y. Ozeki, Y. Hoshino and Y. Tanaka, *Anal. Chem.*, 2019, **91**, 9631–9639.

57 B. G. Saar, C. W. Freudiger, J. Reichman, C. M. Stanley, G. R. Holtom and X. S. Xie, *Science*, 2010, **330**, 1368–1370.

58 Y. Ozeki, W. Umemura, Y. Otsuka, S. Satoh, H. Hashimoto, K. Sumimura, N. Nishizawa, K. Fukui and K. Itoh, *Nat. Photonics*, 2012, **6**, 845–851.

59 Y. Wakisaka, Y. Suzuki, O. Iwata, A. Nakashima, T. Ito, M. Hirose, R. Domon, M. Sugawara, N. Tsumura, H. Watarai, T. Shimobaba, K. Suzuki, K. Goda and Y. Ozeki, *Nat. Microbiol.*, 2016, **1**, 16124.

60 Y. Suzuki, K. Kobayashi, Y. Wakisaka, D. Deng, S. Tanaka, C.-J. Huang, C. Lei, C.-W. Sun, H. Liu, Y. Fujiwaki, S. Lee, A. Isozaki, Y. Kasai, T. Hayakawa, S. Sakuma, F. Arai, K. Koizumi, H. Tezuka, M. Inaba, K. Hiraki, T. Ito, M. Hase, S. Matsusaka, K. Shiba, K. Suga, M. Nishikawa, M. Jona, Y. Yatomi, Y. Yalikun, Y. Tanaka, T. Sugimura, N. Nitta, K. Goda and Y. Ozeki, *Proc. Natl. Acad. Sci. U. S. A.*, 2019, **116**, 15842–15848.

61 C. L. Evans, E. O. Potma, M. Pouris'haag, D. Cote, C. P. Lin and X. S. Xie, *Proc. Natl. Acad. Sci. U. S. A.*, 2005, **102**, 16807–16812.

62 K. Hashimoto, M. Takahashi, T. Ideguchi and K. Goda, *Sci. Rep.*, 2016, **6**, 21036.

63 M. Tamamitsu, Y. Sakaki, T. Nakamura, G. K. Podagatlapalli, T. Ideguchi and K. Goda, *Vib. Spectrosc.*, 2016, **91**, 163–169.

64 D. A. Watson, L. O. Brown, D. F. Gaskill, M. Naivar, S. W. Graves, S. K. Doorn and J. P. Nolan, *Cytometry, Part A*, 2008, **73**, 119–128.

65 Q. Zhang, P. Zhang, H. Gou, C. Mou, W. E. Huang, M. Yang, J. Xu and B. Ma, *Analyst*, 2015, **140**, 6163–6174.

66 K. Hiramatsu, T. Ideguchi, Y. Yonamine, S.-W. Lee, Y. Luo, K. Hashimoto, T. Ito, M. Hase, J.-W. Park, Y. Kasai, S. Sakuma, T. Hayakawa, F. Arai, Y. Hoshino and K. Goda, *Sci. Adv.*, 2019, **5**, eaau0241.